metals

Article

Galvanic Corrosion between Alloy 690 and Magnetite in Alkaline Aqueous Solutions

Soon-Hyeok Jeon, Geun-Dong Song and Do Haeng Hur *

Nuclear Materials Safety Research Division, Korea Atomic Energy Research Institute,
Daejeon 305-353, Korea; E-Mails: junsoon@kaeri.re.kr (S.-H.J.); sgd84@kaeri.re.kr (G.-D.S.)

* Author to whom correspondence should be addressed; E-Mail: dhhur@kaeri.re.kr;
Tel.: +82-42-868-8388; Fax: +82-42-868-8696.

Abstract: The galvanic corrosion behavior of Alloy 690 coupled with magnetite has been investigated in an alkaline solution at 30 °C and 60 °C using a potentiodynamic polarization method and a zero resistance ammeter. The positive current values were recorded in the galvanic couple and the corrosion potential of Alloy 690 was relatively lower. These results indicate that Alloy 690 behaves as the anode of the pair. The galvanic coupling between Alloy 690 and magnetite increased the corrosion rate of Alloy 690. The temperature increase led to an increase in the extent of galvanic effect and a decrease in the stability of passive film. Galvanic effect between Alloy 690 and magnetite is proposed as an additional factor accelerating the corrosion rate of Alloy 690 steam generator tubing in secondary water.

1. Introduction

Nickel-based Alloy 600 has been widely used as a steam generator (SG) heat transfer tubing material in pressurized water reactors (PWRs). However, Alloy 600 tubing experienced various types of corrosion damage, such as stress corrosion cracking, intergranular attack, pitting corrosion, *etc*. Consequently, Alloy 600 has been changed to Alloy 690 with a higher Cr content of about 30% in

weight [1–4]. Although Alloy 690 shows excellent corrosion resistance in PWR environments, it may suffer from corrosion related degradation in high temperature and pressure water [5–9].

Magnetite particles released from the surface of carbon steel piping are transported into an SG, accumulated on the top of tube sheet and deposited on the outer surface of SG tubes. These corrosion products reduce the efficiency of the SG by deterioration of the heat transfer and accelerate the corrosion of SG tubes [10–12]. Magnetite deposited on the Ni-based alloy tube in operating SGs has a porous structure [13,14]. In addition, the magnetite adhering to SG tubes distorts eddy current signals from the tubes during in-service inspection [15].

The surface of Alloy 690 tube is in electrical contact with the porous magnetite deposits. A need exists to know about the galvanic corrosion behavior between Alloy 690 and magnetite in secondary water of PWRs.

To elucidate the galvanic corrosion behaviour between Alloy 690 and magnetite, it is necessary to simulate magnetite deposited on the surface of Alloy 690 in a secondary circuit system. An electrodeposition technique is a simple method to produce a pure magnetite layer on Alloy 690 substrate. Magnetite is produced by a chemical reaction following the oxidation of Fe(II) [16–18] or the reduction of Fe(III) [19,20] at the electrode surface. Recently, Kothari *et al.* [21] have shown that magnetite is easily produced by electrodeposition on a stainless steel substrate in Fe(III)-triethanolamine (TEA) solution at 60–80 °C. Goujon *et al.* [22] characterized magnetite films electrodeposited on the Ni-based alloy and established the optimal temperature and agitation condition for electrodeposition growth of magnetite films in the Fe(III)-TEA solution.

In this study, the galvanic corrosion behavior of Alloy 690 coupled with magnetite was investigated in alkaline aqueous solutions. A magnetite layer was electrodeposited on the surface of Alloy 690 substrate from a Fe(III)-TEA electrolyte. Then, the electrochemical corrosion parameters of Alloy 690 and magnetite were measured under simulated wet layup conditions through electrochemical techniques.

2. Experimental Procedure

2.1. Material Preparation

Alloy 690 was melted in a high frequency vacuum induction furnace, and hot-rolled in a temperature range of 1150–1250 °C. The plates were cold-rolled with a total area reduction of about 70%. The cold-worked samples were annealed at 1100 °C for 5 min followed by water quenching, and then heat-treated at 715 °C for 10 h in a vacuum furnace (Carbolite, Hope valley, UK). Specimens for electrodeposition and electrochemical tests were cut into a dimension of $10 \times 5 \times 1$ mm (length by width by thickness). The specimens were ground to #1000 grit using silicon carbide papers, and then ultrasonically cleaned in acetone and ethanol for 5 min. The chemical composition of Alloy 690 is given in Table 1.

Table 1. Chemical composition of Alloy 690.

Element (wt. %)	C	Cr	Fe	Si	Mn	Ti	Al	Ni
Alloy 690	0.02	28.0	10.2	0.1	0.3	0.1	0.1	Bal.

2.2. Deposition of Magnetite Films

Magnetite films were electrodeposited on Alloy 690 substrates in $Fe_2(SO_4)_3$ solution complexed with TEA. The detailed concentrations in the deposition bath were 0.04 M $Fe_2(SO_4)_3$, 0.1 M TEA, and 2 M NaOH. The solution was prepared by adding $Fe_2(SO_4)_3$ solution to a solution of NaOH and TEA. The electrochemical deposition was carried out in a three electrode cell using a PAR273 potentiostat (Ametek, Berwyn, PA, USA) with Power suite software (Ametek, Berwyn, PA, USA). A saturated calomel electrode (SCE) and a platinum wire were used as a reference and counter electrode, respectively. The SCE was connected via a Luggin capillary whose tip was very close to the surface of the working electrode. The Luggin was cooled through a water cooled spherical condenser so that the temperature of the SCE was maintained at 25 ℃. All electrochemical potentials were given in terms of the SCE at the test temperatures of 30 ℃, 60 ℃, and 80 ℃. Magnetite was electrodeposited in the prepared deposition solution at an applied potential of −1.05 V_{SCE} for 3600 s at 80 ℃.

After electrodeposition, the magnetite films were analyzed using scanning electron microscope (SEM, FEI Company, Hillsboro, OR, USA) and X-ray diffraction (XRD) with a D/Max-2500 X-ray diffractometer (Rigaku, Tokyo, Japan). The magnetite films were also milled by a focused ion beam (FIB) toward the vertical direction of the magnetite surface using a QUANTA 3D FEG FIB-SEM (FEI Company, Hillsboro, OR, USA). Then, the morphology and thickness of the magnetite were analyzed. To calculate the surface area ratio of magnetite/Alloy 690, the surface area of magnetite and Alloy 690 was measured using an Olympus OLS3000 non-contact confocal optical profiler (Olympus, Tokyo, Japan).

2.3. Electrochemical Tests

Two kinds of electrochemical tests were performed: the zero resistance ammetry (ZRA) test and the potentiodynamic polarization test. All test solutions were prepared immediately before each test from high purity demineralized water with the resistivity above 16 MΩ cm. The pH of the solutions at 25 ℃ was adjusted to 9.5 by adding ethanolamine (ETA), which is an organic chemical agent used to control the pH of secondary water in PWRs. The pH of the solution at 60 ℃ was 8.61, which was calculated using the MULTEQ software (EPRI, Palo Alto, CA, USA). Solutions were deaerated by continuously purging with high-purity (99.98%) nitrogen gas at a rate of 600 cm^3/min during the tests. All tests were conducted at 30 ℃ and 60 ℃. These test environments were designed to simulate wet layup conditions of SGs in PWRs.

The ZRA tests were performed using a Reference 600 Potentiostat/galvanostat/ZRA (Gamry, Warminster, PA, USA) embedded with Gamry framework system. An SCE was used as a reference electrode. Alloy 690 specimen was connected to the working electrode and the magnetite specimen was connected to the counter electrode. After the open circuit potential (OCP) was stabilized, the specimens were electrically connected though the ZRA. The variation of galvanic potential (E_{couple}) and galvanic current density (i_{couple}) of Alloy 690 coupled with magnetite was measured during 3600 s.

The potentiodynamic polarization tests were carried out using a PAR273 potentiostat (Ametek, Berwyn, PA, USA) with Power suite software (Ametek, Berwyn, PA, USA). An SCE and a platinum wire were used as a reference and counter electrode, respectively. After the OCP was stabilized, a

polarization scan was started from the OCP to the cathodic or anodic direction with a scan rate of 1 mV/s. Therefore, each cathodic and anodic polarization curve was obtained from a newly prepared sample. The corrosion rates of Alloy 690 and magnetite were determined by means of the Tafel extrapolation method. The E_{couple} and the i_{couple} of the pair were calculated from the potentiodynamic polarization curves based on the mixed potential theory. All electrochemical tests were conducted at least three times on separate specimens to verify reproducibility. Good reproducibility was confirmed.

3. Results and Discussion

3.1. Electrodeposition of Magnetite

Figure 1 shows a linear sweep voltammogram for Alloy 690 substrate in the electrodeposition solution with Fe(III)-TEA at 80 °C. The potential was scanned from the OCP of −0.8 V_{SCE} down to −1.3 V_{SCE} at a scan rate of 40 mV/s. The electrochemical reduction of Fe(III)-TEA was observed at negative potentials below approximately −1.00 V_{SCE}. The first reduction wave of this linear sweep was measured approximately between −1.00 and −1.20 V_{SCE}. The second reduction wave was also observed in the potential range from −1.20 to −1.30 V_{SCE}.
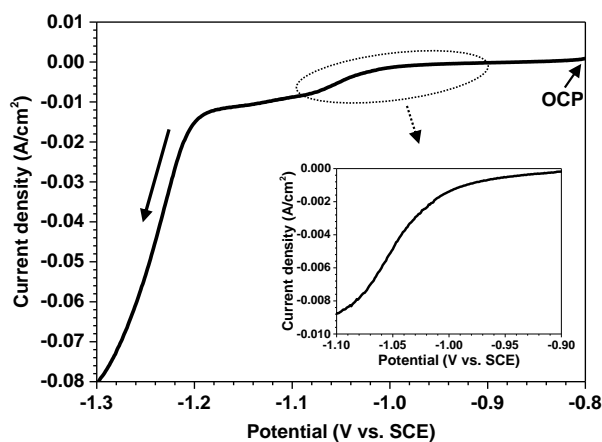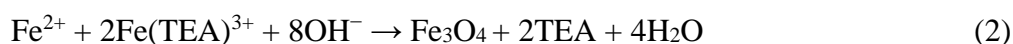

Figure 1. Linear sweep voltammogram of Alloy 690 substrate in Fe(III)-TEA deposition solution at 80 °C.

The electrodeposition of magnetite film in a Fe(III)-TEA solution can be simplified by two steps. The first step is that the Fe(III)-TEA solution is electrochemically reduced to Fe^{2+} and TEA. The second step is that the electrochemically produced Fe^{2+} reacts chemically with Fe(III)-TEA solution to produce magnetite film. The proposed mechanism is expressed in the following reactions (1) and (2) [21–24].

$$Fe(TEA)^{3+} + e^{-} \rightarrow Fe^{2+} + TEA \tag{1}$$

$$Fe^{2+} + 2Fe(TEA)^{3+} + 8OH^{-} \rightarrow Fe_3O_4 + 2TEA + 4H_2O \tag{2}$$

Therefore, the first reduction wave observed between −0.95 and −1.20 V_{SCE} can be attributed to a one electron exchange reaction corresponding to the above reaction (1) [23]. On the contrary, the second reduction wave between −1.20 and −1.30 V_{SCE} seems to be due to a two-electron process corresponding to the reduction of Fe(II) to Fe [22–24]. In this work, the magnetite film was

electrodeposited on Alloy 690 substrate in the Fe(III)-TEA solution at the potential of −1.05 V$_{SCE}$ (first reduction wave region) for 3600 s.

Figure 2 shows the SEM images of the magnetite electrodeposited on the Alloy 690 substrate. The surface of magnetite has a dense and highly faceted morphology, which is homogeneous on the entire surface of the deposit (Figure 2a). Figure 2b presents the FIB-SEM image of cross sectional electrodeposited magnetite film on the Alloy 690 substrate. The thickness of the magnetite film ranged from 0.8 to 1.5 μm, with an average of 1.2 μm. No defects, such as holes or cracks, could be observed at the interface between the Alloy 690 substrate and magnetite, confirming that magnetite film was tightly bonded to Alloy 690 substrate.
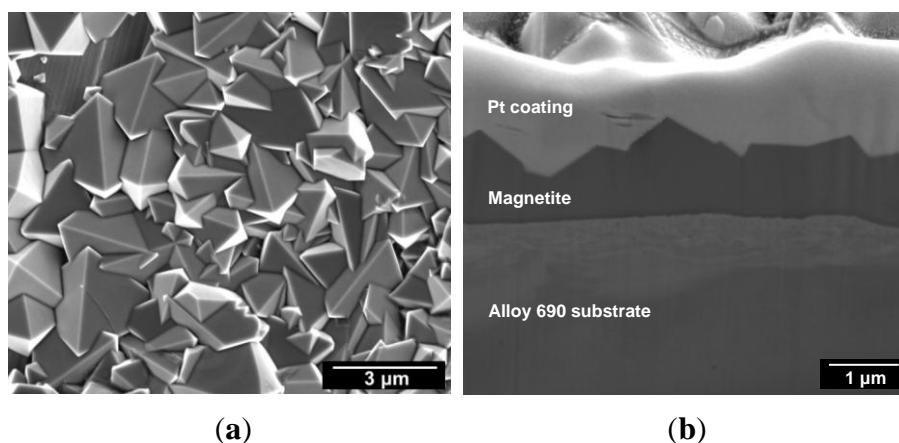

(**a**)   (**b**)

Figure 2. Magnetite film electrodeposited on the Alloy 690 substrate; (**a**) surface of magnetite film and (**b**) cross section of magnetite film.

Figure 3 shows the XRD analysis of the magnetite electrodeposited on the Alloy 690 substrate. The magnetite film is all crystalline, and all peaks correspond to magnetite film.
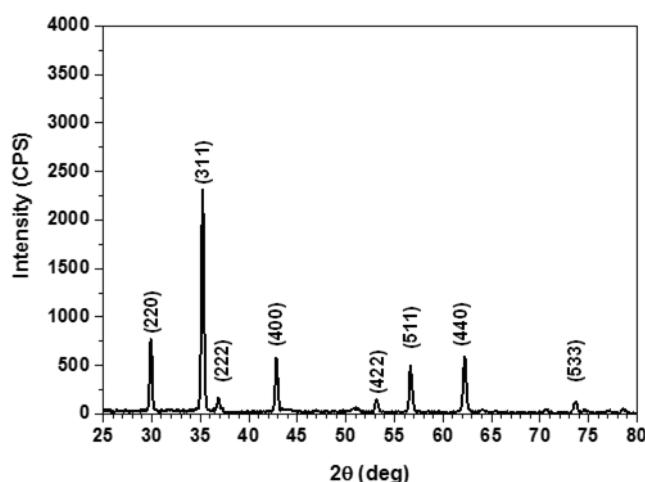

Figure 3. XRD pattern of magnetite film electrodeposited on Alloy 690 substrate.

Figure 4 shows the surface morphologies of Alloy 690 and electrodeposited magnetite specimen through the confocal optical profiler. The deposited magnetite shows a rougher surface than the Alloy 690 sample. The measured surface area ratio of magnetite to Alloy 690 was about 1.3. Originally, we

prepared all specimens with the same nominal dimension. In a microscopic manner, however, magnetite specimens have a larger real surface area participating in a corrosion process. Therefore, it should be noted that all electrochemical data in this paper were measured under the condition that the area ratio of magnetite to Alloy 690 was 1.3.
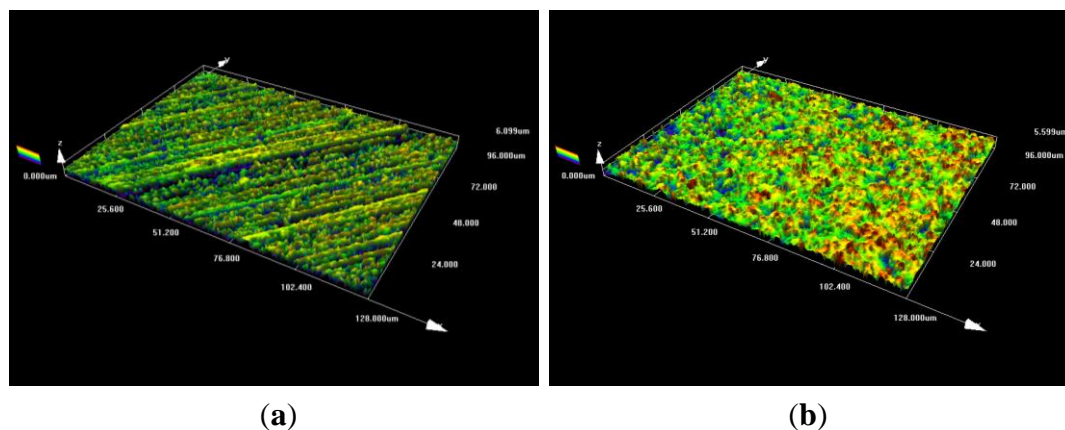

<div align="center">(a)   (b)</div>

Figure 4. Surface morphology using a non-contact confocal optical profiler; (**a**) Alloy 690 and (**b**) magnetite film.

3.2. Electrochemical Behavior of Alloy 690 and Magnetite

Figure 5 shows the corrosion potential (E_{corr}) and the galvanic potential (E_{couple}) of Alloy 690 and magnetite in the alkaline solution with pH 9.5 at 30 ℃ and 60 ℃ as a function of time. The E_{corr} of the magnetite was nobler than that of Alloy 690, whereas the E_{couple} of magnetite/Alloy 690 couple is between the E_{corr} of the magnetite and Alloy 690. Accordingly, magnetite will behave as the cathode of the galvanic couple, while Alloy 690 will be the anode and is expected to undergo excessive corrosion. In addition, as the temperature increased from 30 ℃ to 60 ℃, the E_{corr} of both Alloy 690 and magnetite and E_{couple} decreased.

Figure 6 shows the galvanic current density (i_{couple}) of Alloy 690 coupled with magnetite in the alkaline solution with pH 9.5 at 30 ℃ and 60 ℃ using ZRA. In the Alloy 690/magnetite couple, the i_{couple} of Alloy 690 was the positive value corresponding to the oxidation reaction, indicating that Alloy 690 specimen was the anode of the couple. The i_{couple} of the Alloy 690 specimen is high initially and decreases considerably with time to an extremely low current density. This decrease in i_{couple} with time can be attributed to the formation of passive film on the surface of Alloy 690. The i_{couple} tends to diminish as the metal passivates by oxide film growth during the initial stage and to stabilize from the final stage [25]. The i_{couple} increased when the temperature increased from 30 ℃ to 60 ℃. Especially, during the formation of passive film at 60 ℃, the current density transients were observed from the curve of i_{couple} (Figure 6b). These kind of transients was related to the nucleation of metastable pits, which were immediately repassivated [26–28]. These ZRA results indicate that the increase in temperature leads to an increase in the extent of galvanic effect and a decrease in the stability of passive film.
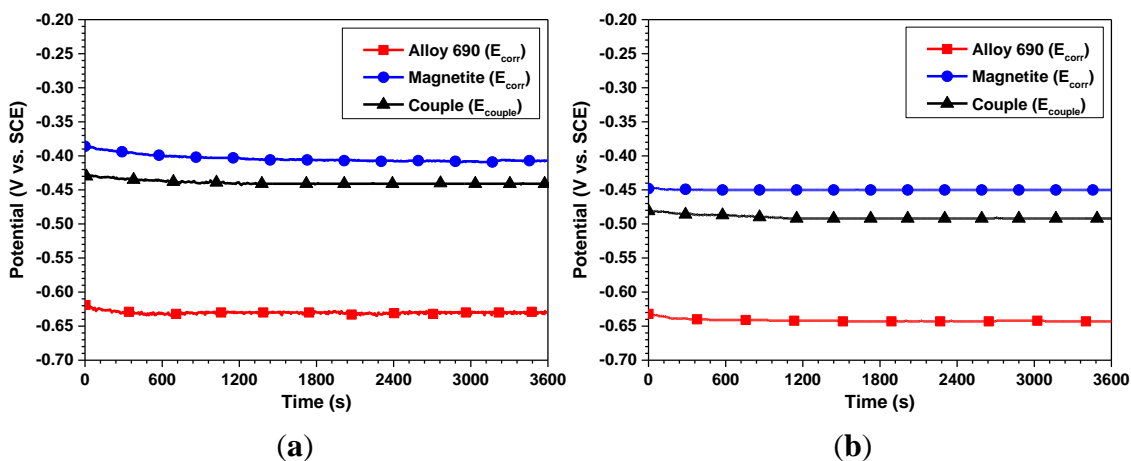
Figure 5. Corrosion potential and galvanic potential of Alloy 690 and electrodeposited magnetite in the alkaline solution with pH 9.5 at (**a**) 30 ℃ and (**b**) 60 ℃.
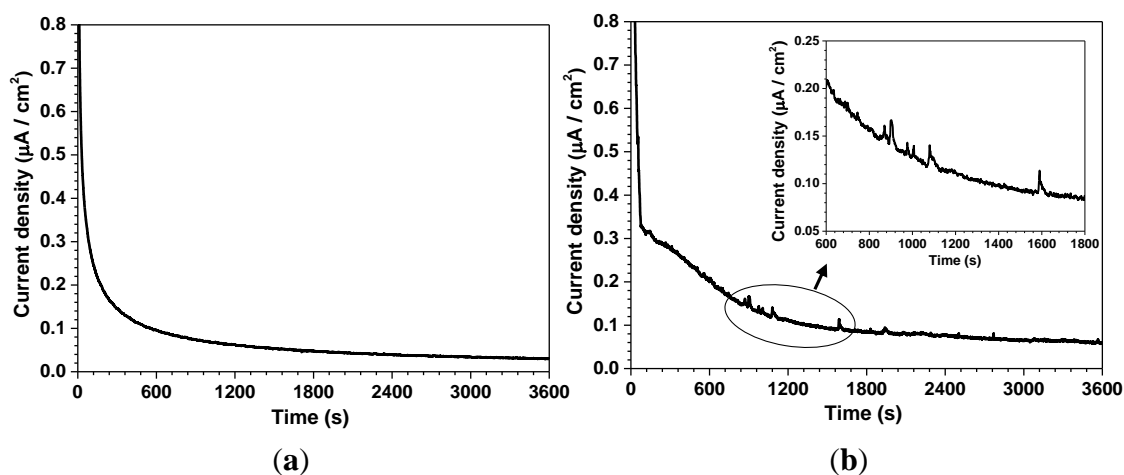

Figure 6. Galvanic current density of Alloy 690 coupled with electrodeposited magnetite in the alkaline solution with pH 9.5 at (**a**) 30 ℃ and (**b**) 60 ℃.

Figure 7 shows the potentiodynamic polarization curves of Alloy 690 and magnetite in the alkaline solution with pH 9.5 at 30 ℃ and 60 ℃. The corrosion current density (i_{corr}) of Alloy 690 and magnetite was calculated by means of the Tafel extrapolation method. The galvanic potential (E_{couple}) and the galvanic current density (i_{couple}) of the pair were also determined using the mixed potential theory. These electrochemical corrosion parameters are summarized in Table 2. The E_{corr} of magnetite was higher than that of Alloy 690. The i_{corr} of Alloy 690 was lower than that of magnetite. In addition, as the temperature increased from 30 ℃ to 60 ℃, the i_{corr} of both Alloy 690 and magnetite and i_{couple} increased.

When magnetite and Alloy 690 are electrically coupled, the corrosion rate of coupled Alloy 690 at 60 ℃ will increase by about 2.6 times than that of non-coupled Alloy 690 due to the shift in its potential in the positive direction. In cathodic reaction, the reductive dissolution of magnetite and formation of dissolved ferrous or ferrous species will occur according to Equation (3) as well as the hydrogen evolution reaction [29]. Jung *et al*. [29] showed that the reductive dissolution of magnetite occurred in the alkalized reducing condition.

$$Fe_3O_4 + 2H_2O + 2H^+ + 2e^- \rightarrow 3Fe(OH)_2 \tag{3}$$
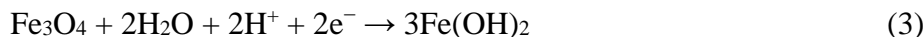
The i_{couple} increased when the temperature was changed from 30 ℃ to 60 ℃. This result means that temperature promotes the galvanic corrosion rate of coupled Alloy 690. It is because higher temperature can promote the ion transport and decrease the pH and then accelerate the corrosion. These results calculated from the mixed potential theory show a very similar tendency to the results obtained from the ZRA tests.
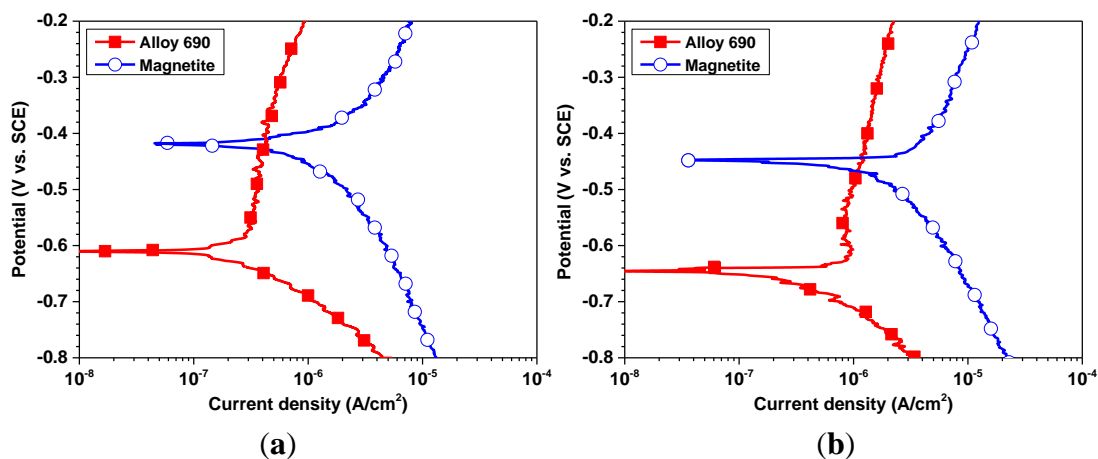

Figure 7. Potentiodynamic polarization curves of Alloy 690 and electrodeposited magnetite in the alkaline solution with pH 9.5 at (**a**) 30 ℃ and (**b**) 60 ℃.

Table 2. Electrochemical corrosion parameters of Alloy 690 and magnetite obtained from potentiodynamic polarization curves in the alkaline solution with pH 9.5.

Corrosion parameters	30 ℃		60 ℃	
	Alloy 690	**Magnetite**	**Alloy 690**	**Magnetite**
E_{corr} (V_{SCE})	−0.610 ±0.012	−0.418 ±0.008	−0.647 ±0.014	−0.445 ±0.004
E_{couple} (V_{SCE})	−0.432 ±0.005		−0.469 ±0.010	
i_{corr} ($\mu A/cm^2$)	0.21 ±0.02	0.79 ±0.08	0.41 ±0.05	1.31 ±0.11
i_{couple} ($\mu A/cm^2$)	0.39 ±0.10		1.08 ±0.17	

In general, an increase in temperature is expected within the magnetite deposited on the outer surface of Alloy 690 tubing due to the deterioration of heat transfer efficiency from the primary to secondary side. Increasing the temperature leads to an increase in the solubility of impurities until the pressurized water approaches the super-saturation, forming a corrosive environment in the porous magnetite deposits. Especially, the aggressive ionic species such as chloride, sulfate and sodium have been reported to accelerate the corrosion degradation of nickel-based SG tubing [30]. Magnetite deposited on Alloy 690 tubes in operating SG has a porous structure [14,15]. Therefore, the surface of Alloy 690 tubes is in galvanic contact with the porous magnetite deposits. In addition, the surface area ratio of the cathode to anode on the outer surface of steam generator tubes covered with the porous magnetite is much larger than the area ratio of this experimental condition. Consequently, the corrosion rate of Alloy 690 tubes in operating steam generators is accelerated.

This study demonstrates that the corrosion rate of Alloy 690 increases by a galvanic couple with magnetite. Figure 8 shows the schematic of mechanism for the galvanic effect on the corrosion rate of Alloy 690 tubing coupled with magnetite. The corrosion rate of Alloy 690 SG tubing is additionally accelerated by a galvanic effect as well as by the concentration effect of aggressive chemical impurities.
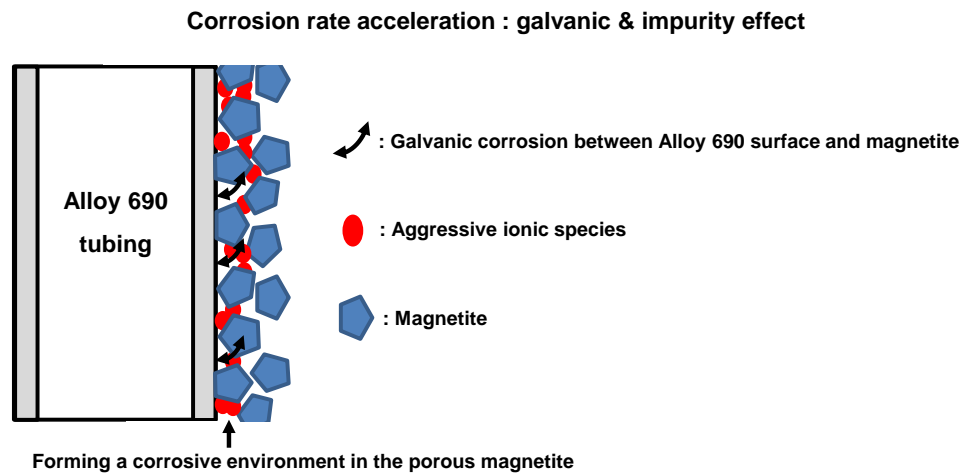

Figure 8. Schematic of the galvanic corrosion between Alloy 690 tubing and magnetite.

4. Conclusions

The galvanic corrosion behavior of Alloy 690 coupled with magnetite in alkaline aqueous solutions was predicted by the mixed potential theory and verified by ZRA measurements. The potential differences between Alloy 690 and magnetite and the sign of the galvanic current of the couple indicated that Alloy 690 was the anode of the galvanic pair. Galvanic coupling increased the corrosion rate of Alloy 690 due to the shift in its potential to the anodic direction. The extent of galvanic effect between Alloy 690 and magnetite increased with increasing temperature from 30 ℃ to 60 ℃. Therefore, the galvanic effect between Alloy 690 and magnetite should be considered as an additional factor accelerating the corrosion rate of Alloy 690 SG tubing in secondary water.

Author Contributions

Soon-Hyeok Jeon is the first author of the paper and performed the experimental tests of the Alloy 690 and magnetite. Geun-Dong Song supported experimental tests and microstructure analyses.

Do-Haeng Hur is the corresponding author of the paper, conceived the paper, and supervised the experimental tests and microstructure analysis.

Conflicts of Interest

The authors declare no conflict of interest.

References

1. Dutta, R.S. Corrosion aspects of Ni-Cr-Fe based and Ni-Cu based steam generator tube materials. *J. Nucl. Mater.* **2009**, *393*, 343–349.
2. Ziemniak, S.E.; Guilmette, P.A.; Turcotte, R.A.; Tunison, H.M. Oxidative dissolution of nickel metal in hydrogenated hydrothermal solutions. *Corros. Sci.* **2008**, *50*, 449–462.
3. Zagal, J.M.; Lopez, H.F.; Flores, O.; Albarran, J.L.; Martinez, L. Microstructural effects on the hydrogen permeation of an Inconel alloy 690. *Corros. Sci.* **2008**, *50*, 3371–3377.
4. Pandey, M.D.; Datla, S.; Tapping, R.L.; Lu, Y.C. The estimation of lifetime distribution of Alloy 800 steam generator tubing. *Nucl. Eng. Des.* **2009**, *239*, 1862–1869.
5. Zhong, X.Y.; Han, E.H.; Wu, X.Q. Corrosion behavior of Alloy 690 in aerated supercritical water. *Corros. Sci.* **2013**, *66*, 369–379.
6. Zhang, Z.; Wang, J.; Han, E.H.; Ke, W. Influence of dissolved oxygen on oxide films of Alloy 690TT with different surface status in simulated primary water. *Corros. Sci.* **2011**, *53*, 3623–3635.
7. Kuang, W.; Wu, X.; Han, E.H.; Rao, J. The mechanism of oxide film formation on Alloy 690 in oxygenated high temperature water. *Corros. Sci.* **2011**, *53*, 3853–3860.
8. Kuang, W.; Wu, X.; Han, E.H. Influence of dissolved oxygen concentration on the oxide film formed on Alloy 690 in high temperature water. *Corros. Sci.* **2013**, *69*, 197–204.
9. Huang, F.; Wang, J.; Han, E.H.; Ke, W. Microstructural characteristics of the oxide films formed on Alloy 690 TT in pure and primary water at 325 °C. *Corros. Sci.* **2013**, *76*, 52–59.
10. Plonski, I.H. Effect of bare metal surface on the dissolution in aqueous citrate solutions of magnetite films on carbon steel. *J. Appl. Electrochem.* **1997**, *27*, 1184–1192.
11. Ramesh, C.; Murugesan, N.; Prince, A.A.M.; Velmurugan, S.; Narasimhan, S.V.; Ganesan, V. Application of polymer electrolyte based hydrogen sensor to study corrosion of carbon steel in acid medium. *Corros. Sci.* **2001**, *43*, 1865–1875.
12. Prince, A.A.M.; Velmurugan, S.; Narasimhan, S.V.; Ramesh, C.; Murugesan, N.; Raghavan, P.S.; Gopalan, R. Dissolution behaviour of magnetite film formed over carbon steel in dilute organic acid media. *Nucl. Mater.* **2001**, *289*, 281–290.
13. Gonzalez, F.; Spekkens, P. Concentration Processes under Tubesheet Sludge Piles in Nuclear Steam Generators. *Nucl. J. Can.* **1987**, *1*, 129–140
14. Manahan, M.P. Mechanical behaviour of magnetite from the Oconee-2 and TMI-1 steam generators using miniaturized specimen technology. *J. Sci.* **1990**, *25*, 3415–3423.
15. Hur, D.H.; Choi, M.S.; Kim, U.C.; Han, J.H. Magnetite dissolution and corrosion behavior in high temperature EDTA solvents. *Nucl. Eng. Des.* **2003**, *220*, 11–16.
16. Carlier, D.; Terrier, C.; Arm, C.; Anserment, J.P. Preparation and magnetic properties of Fe_3O_4 nanostructures grown by electrodeposition. *Electrochem. Solid State Lett.* **2005**, *8*, 43–46.

17. Peulon, S.; Antony, H.; Legrand, L.; Chausse, A. Thin layers of iron corrosion products electrochemically deposited on inert substrates: Synthesis and behavior. *Electrochim. Acta* **2004**, *49*, 2891–2899.

18. Ho, S.Y.; Wang, K.C.; Kuo, S.L.; Wu, N.L. Investigation on capacitance mechanisms of Fe_3O_4 electrochemical capacitors. *Electrochem. Soc.* 2006, *153*, A75–A80.

19. Teng, C.L.; Ryan, M.P. A morphological study of nanocrystalline magnetite electrodeposited onto polycrystalline copper substrates. *Electrochem. Solid State Lett.* **2007**, *10*, 108–112.

20. Mitra, S.; Poizot, P.; Finke, A.; Tarascon, J.M. Growth and electrochemical characterization versus lithium of Fe_3O_4 electrodes made by electrodeposition. *Adv. Funct. Mater.* **2006**, *16*, 2281–2287.

21. Kothari, H.M.; Kulp, E.A.; Limmer, S.J.; Poizot, P.; Bohannan, E.W.; Switzer, J.A. Electrochemical deposition and characterization of Fe_3O_4 films produced by the reduction of Fe(III)-triethanolamine. *J. Mater. Res.* **2006**, *21*, 293–301.

22. Goujon, C.; Pauporté, T.; Mansour, C.; Delaunary, S.; Bretelle, J.L. Electrochemical deposition of thick iron oxide films on nickel based supperalloy substrates. *Electrochim. Acta* **2015**, *176*, 230–239.

23. Kulp, E.A.; Kothari, H.M.; Limmer, S.J.; Yang, J.; Gudavarthy, R.V.; Bohannan, E.W.; Switzer, J.A. Electrodeposition of epitaxial magnetite films and ferrihydrite nanoribbons on single-crystal gold. *Chem. Mater.* **2009**, *21*, 5022–5031.

24. Mohr, S.; Bechtold, T. Electrochemical behaviour of iron-complexes in presence of competitive ligands: A strategy for optimization of current density. *J. Appl. Electrochem.* **2001**, *31*, 363–368.

25. Burstein, G.T.; Liu, C.; Souto, R.M. The effect of temperature on the nucleation of corrosion pits on titanium in Ringer's physiological solution. *Biomaterials* **2005**, *26*, 245–256.

26. Ilevbare, G.O.; Burstein, G.T. The role of alloyed molybdenum in the inhibition of pitting corrosion in stainless steels. *Corros. Sci.* **2001**, *43*, 485–513.

27. Burstein, G.T.; Liu, C. Nucleation of corrosion pits in Ringer's solution containing bovine serum. *Corros. Sci.* **2007**, *49*, 4296–4306.

28. Burstein, G.T.; Liu, C. Depassivation current transients measured between identical twin microelectrodes in open circuit. *Corros. Sci.* **2008**, *50*, 2–7.

29. Jung, K.S.; Sung, K.W. *Magnetite: Structure, Properties and Applications*; Nova Science Publishers: New York, NY, USA, 2010; pp. 261–298.

30. Steahle, R.W.; Gorman, J.A. Quantitative assessment of submodes of stress corrosion cracking on the secondary side of steam generator tubing in pressurized water reactors: Part I. *Corrosion* **2003**, *59*, 931–994.